ELSEVIER

Bottom-up, scalable synthesis of anatase nanofilament-based two-dimensional titanium carbo-oxide flakes

Hussein O. Badr [1], Tarek El-Melegy [1], Michael Carey [1], Varun Natu [1], Mary Q. Hassig [1], Craig Johnson [2], Qian Qian [1], Christopher Y. Li [1], Kateryna Kushnir [3], Erika Colin-Ulloa [3], Lyubov V. Titova [3], Julia L. Martin [4], Ronald L. Grimm [4], Rahul Pai [5], Vibha Kalra [5], Avishek Karmakar [1], Anthony Ruffino [6], Stefan Masiuk [6], Kun Liang [7], Michael Naguib [7], Olivia Wilson [1], Andrew Magenau [1], Kiana Montazeri [1], Yucheng Zhu [1], Hao Cheng [1], Takeshi Torita [8], Masashi Koyanagi [8], Akimaro Yanagimachi [8], Thierry Ouisse [9], Maxime Barbier [9,10], Fabrice Wilhelm [10], Andrei Rogalev [10], Jonas Björk [11], Per O.Å. Persson [11], Johanna Rosen [11], Yong-Jie Hu [1,*], Michel W. Barsoum [1,11,*]

[1] Department of Material Science and Engineering, Drexel University, Philadelphia, PA, USA
[2] Materials Characterization Core, Drexel University, Philadelphia, PA, USA
[3] Department of Physics, Worcester Polytechnic Institute, Worcester, MA, USA
[4] Department of Chemistry & Biochemistry, Worcester Polytechnic Institute, Worcester, MA, USA
[5] Department of Chemical & Biological Engineering, Drexel University, Philadelphia, PA, USA
[6] Department of Mechanical Engineering and Mechanics, Drexel University, Philadelphia, PA, USA
[7] Department of Physics and Engineering Physics, Tulane University, New Orleans, LA, USA
[8] Murata Manufacturing Co., Ltd, Nagaokakyo-shi, Kyoto, Japan
[9] Univ. Grenoble Alpes, CNRS, Grenoble INP, LMGP, F-38000 Grenoble, France
[10] European Synchrotron Radiation Facility (ESRF), Grenoble, France
[11] Thin Film Physics Division, Department of Physics, Chemistry and Biology (IFM), Linköping University, Linköping, Sweden

Two-dimensional (2D) materials offer advantages that their 3D counterparts do not. The conventional method for the bulk synthesis of 2D materials has predominantly been through etching layered solids. Herein, we convert – through a bottom-up approach – 10 binary and ternary titanium carbides, nitrides, borides, phosphides, and silicides into 2D flakes by immersing them in a tetramethylammonium hydroxide solution at temperatures in the 25–85 °C range. Based on X-ray diffraction, density functional theory, X-ray photoelectron, electron energy loss, Raman, X-ray absorption near edge structure spectroscopies, transmission and scanning electron microscope images and selected area diffraction, we conclude that the resulting flakes are carbon containing anatase-based layers that are, in turn, comprised of $\approx 6 \times 10$ Å^2 nanofilaments in cross-section some of which are few microns long. Electrodes made from some of these films performed well in lithium-ion and lithium-sulphur systems. These materials also reduce the viability of cancer cells thus showing potential in biomedical applications. Synthesizing 2D materials, at near ambient conditions, with non-layered, inexpensive,

* Corresponding authors.
E-mail addresses: Hu, Y.-J. (yh593@drexel.edu), Barsoum, M.W. (barsoumw@drexel.edu).

 https://doi.org/10.1016/j.mattod.2021.10.033

green precursors (e.g., TiC) is paradigm shifting and will undoubtedly open new and exciting avenues of research and applications.

Keywords: Layered solids; 2D flakes; Nanofilaments; Self-assembly; Organic salts; Bottom-up; Energy storage

Introduction

One and two-dimensional (2D) materials offer advantages that their 3D counterparts do not such as very high specific surface areas, quantum size effects, and customizable termination states [1,2]. Historically, the starting point for synthesizing 2D materials in bulk has mainly been layered solids, be they clays, graphite, or more recently, MAX phases [3–8]. Bulk 2D materials are often produced in a top-down approach by exfoliating or etching layered precursors [3–7,9]. For example, in 2011, we selectively etched Al from MAX phases to produce MXenes [6]. Growing micron-sized truly 2D oxide flakes, however, has remained a major challenge [10,11]. Further, synthesizing 2D materials in large scale from non-layered solids, in a single step, was deemed difficult, if not impossible.

The genesis of this work was rooted in our attempts to selectively etch MAX phases without the use of fluorine. Xuan et al. pre-etched the MAX phase, Ti_3AlC_2, with HF and immersed the powders in a tetramethylammonium hydroxide (TMAH) solution and claimed to have produced MXenes [12]. Instead we obtained anatase-based 2D titanium carbo-oxides, henceforth referred to as TCOs that demonstrate stoichiometries and structures that radically depart from other literature reports [13]. Herein, we immersed 10 different water insoluble binary and ternary carbides, nitrides, borides, phosphides, and silicides in 25 wt.% TMAH aqueous solutions at 25–85 °C and converted them into 2D flakes, that are comprised of nanofilaments (nfs), some of which, depending on precursor, were electrically conductive. A schematic of the overall process is shown in Fig. 1a. Table S1 in Supplementary Materials (SM) lists all the precursors and ingredients used. Table S2 summarizes the conditions used in 31 separate reactions. In all cases, colloidal suspensions were produced that after washing and filtering produced free-standing filtered films, (FF).

Results and discussion

In all cases, except when TiO_2 was the precursor, 2D flakes were obtained. A typical cross-sectional scanning electron microscope (SEM) image of a TiC-derived film (Fig. 1b) clearly showed the 2D nature of the FFs. This micrograph is especially revealing in that it shows both undigested TiC particles (bottom right) and flakes. A colloidal suspension, with concentrations in the 10 g/L range, is shown in inset in Fig. 1b. SEM images of other films are shown in Fig. S1. The FFs varied in color from light to dark gray. The fact that these flakes can be synthesized from non-layered precursors and result in FF that are structurally and chemically similar is strong evidence for a bottom-up approach. In our interpretation, TMAH acts as a near-universal solvent that dissolves the precursor and releases Ti atoms that spontaneously react with C and O in the TMAH/water to form 2D flakes comprised of self-

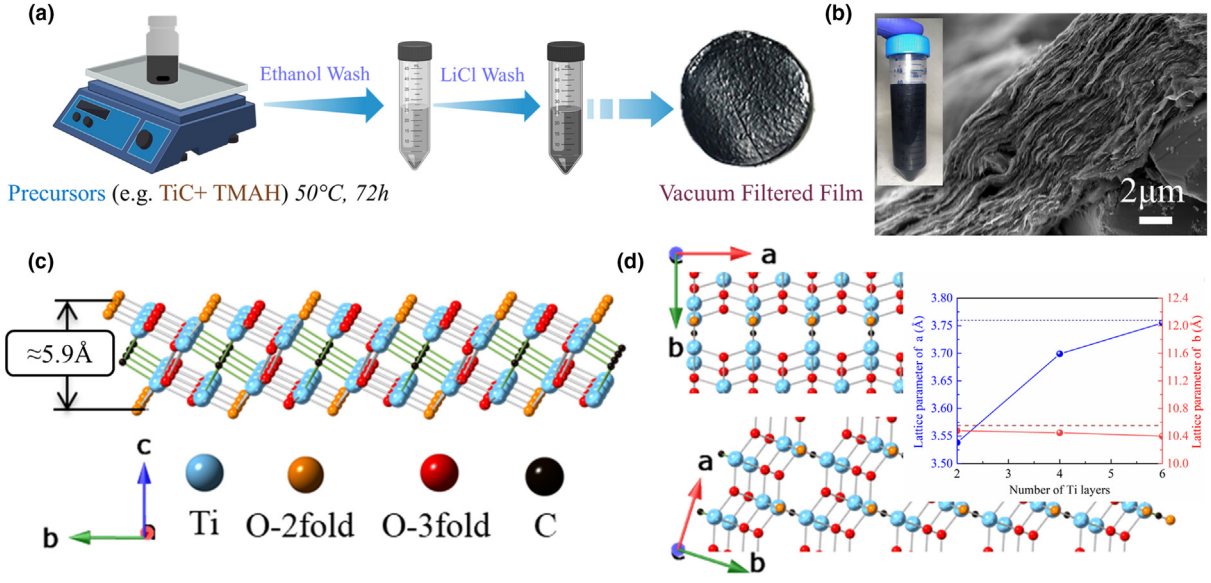

FIGURE 1

Fabrication process, SEM micrographs and DFT structures. (a) Schematic of fabrication process, (b) Typical cross-sectional SEM micrograph of a TiC-derived FF. Note undigested TiC particles in bottom right corner. Inset shows pictures of typical colloidal suspension. (c) Isometric side view of 4 Ti-layered 2D anatase-based structure with Ti_4O_6C chemistry that best fits XRD and SAD results. Blue, orange, red, and black spheres represent Ti, 2- and 3-fold coordinated O, and C respectively. Vertical arrow on left denotes approximate dimension; (d) Top view of nfs growing in [200] (top) and [110] (bottom) directions. Inset in (d) compares experimental LPs (dashed lines) with DFT predictions (solid lines) as a function of number of Ti layers. Our coordinate system is shown in lower left in c and d and is *not* that of bulk anatase (see SM crystallography section).

assembled nfs (see below). The TMAH role is thus twofold: *solvent and templating agent.*

A X-ray diffraction (XRD) pattern of a Ti_3AlC_2-derived film after ethanol washing (inset in Fig. 2a) is typical of 2D materials [7,9]. XRD patterns of dry FF obtained from other precursors are shown in Fig. S2. The absence, for the most part, of peaks associated with the precursors is noteworthy. To gain insight into the underlying structure we obtained XRD patterns (Fig. 2a) on a vertically oriented FF [14] (see Fig. S3a) that was obtained after heating Ti_3AlC_2 for 3 days at 50 °C then washed with ethanol and water. The red vertical lines were obtained as follows: First, the *c*-lattice parameter, LP, was calculated from the horizontally oriented films (inset in Fig. 2a). The structure shown in Fig. 1c was then used to calculate the position of *all* peaks. All planes with non-zero *l* indices were eliminated, leaving the red lines. The good agreement between the density functional theory (DFT) generated LPs and the experimental ones (inset in Fig. 1d) lends credence that we are dealing with a 4 Ti-layered anatase-based 2D material (see below). Patterns for other vertically oriented films, derived from other precursors, are shown in Fig. S3b. In all cases, peaks – *with identical angles* - were obtained. This is crucial and cannot be overemphasized since it demonstrates that precursor chemistry does not alter the ultimate structures formed, including their LPs.

Transmission electron microscope (TEM) images of TiC-, Ti_3SiC_2-, and Ti_3AlC_2-derived flakes revealed the presence of 2D flakes some of which were > 1 μm in lateral sizes (Fig. 3a; Fig. S4). Selected area diffraction (SAD) of the latter in some regions resulted in 3 main rings (see insets in Figs. S4b and c). When the ring *d-spacings* were converted to 2θ values, (blue squares in Fig. 2a) good agreement with the XRD peaks was found confirming our SAD patterns are *representative* (For more results see Table S3). More interestingly, in other regions, two sets of arcs (insets in Fig. 3a and Fig. S4a) were observed. One set of arcs indicated that the long axis of the nfs is in the [110] direction; the other in the [200] direction (see Fig. 1d). The angle between them is shown in

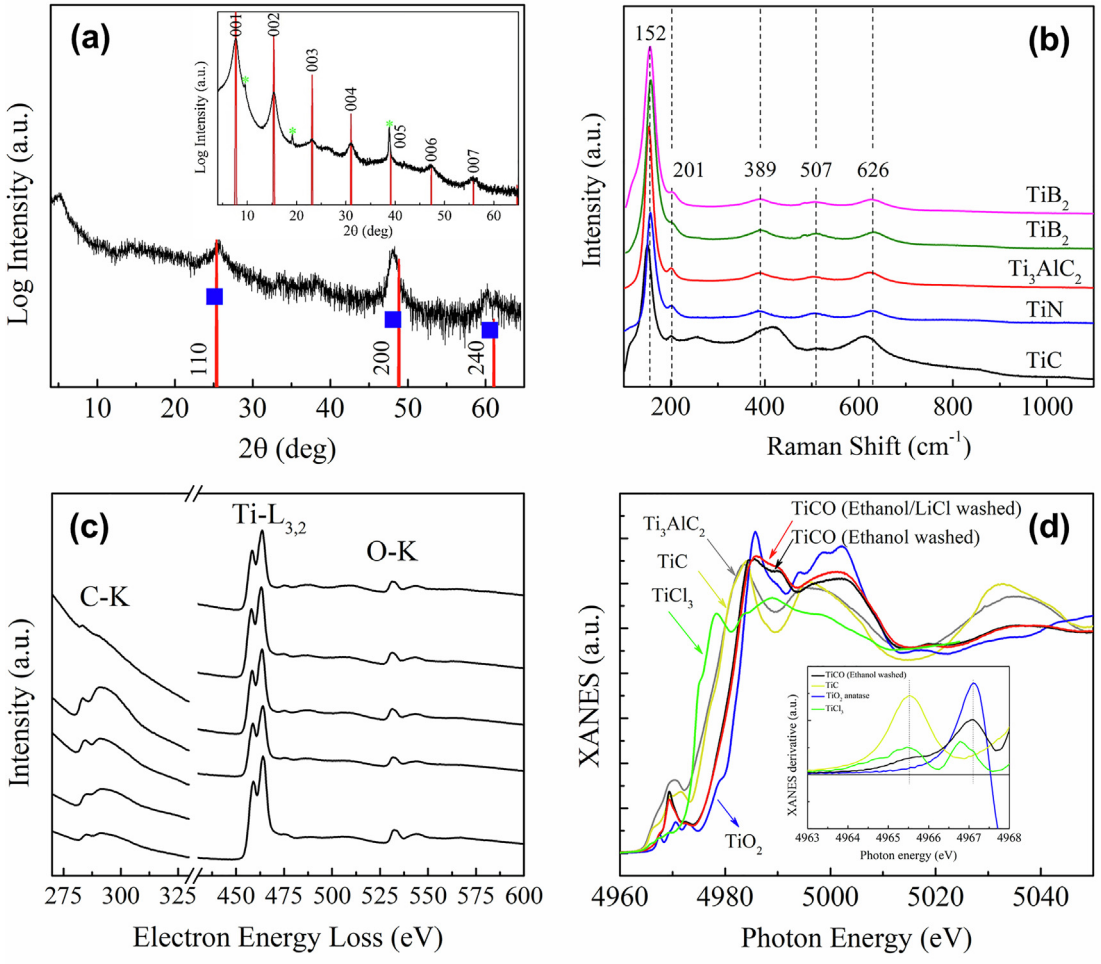

FIGURE 2

Characterization of 2D material. (a) XRD patterns, on log scale, of filtered, vertically oriented, Ti_3AlC_2-derived film in transmission mode. Inset shows pattern of horizontally oriented film. 5° 2θ peak is due to Kapton tape. Blue squares are 2θ locations determined from TEM-SAD patterns (Table S3). (b) Raman spectrum of FFs obtained from precursors indicated. All powders heated at 50 °C for 3 d and washed with ethanol and water, except the top TiB_2 that was produced at 80 °C for 2 d. All peaks belong to anatase.[15] (c) Core loss EELS data measured from 5 individual particles. Graph shows carbon –K edge at ~280 eV energy loss, titanium $-L_{3,2}$ peaks at ~450 eV energy loss and oxygen –K edge at ~530 eV energy loss. All spectra are normalized to the Ti edge peak intensity and are vertically separated for clarity. (d) XANES results of TiC-derived films together with those for anatase, Ti_3AlC_2, TiC and $TiCl_3$. Both TiC samples were reacted in TMAH at 50 °C for 3d. Inset shows XANES derivative.

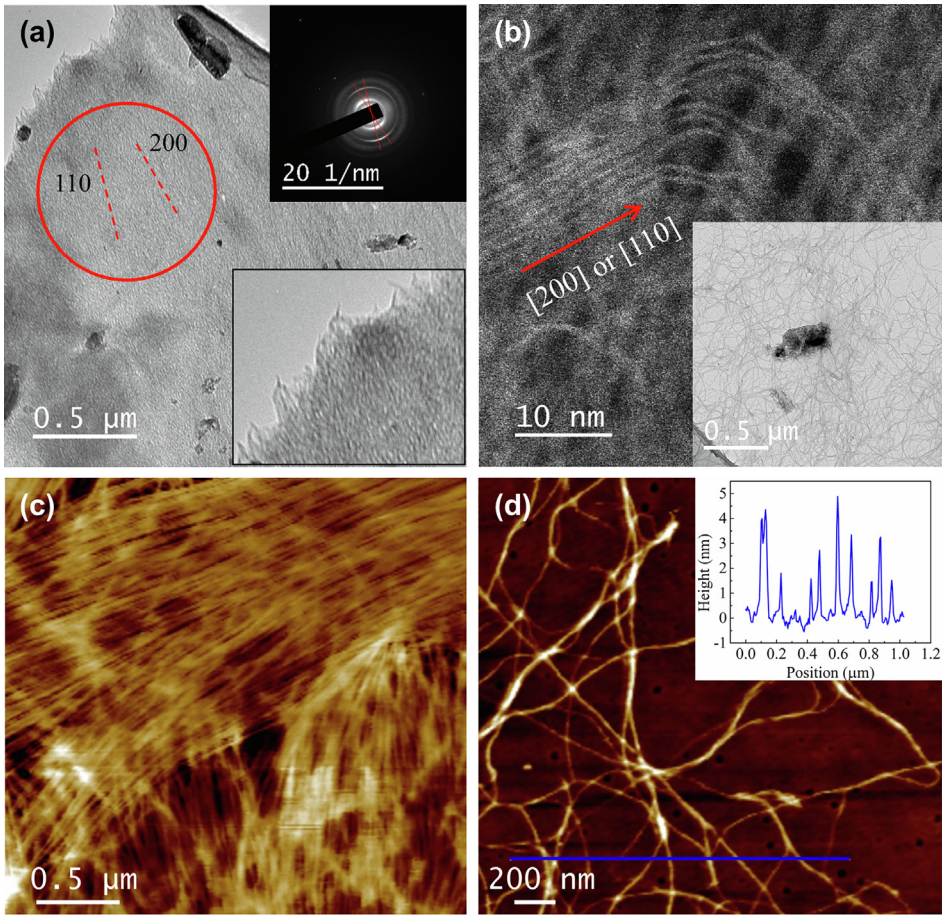

FIGURE 3

TCO Flake morphology. (a) Typical TEM image of TCO flake > 4 μm in lateral size. SAD of area encircled in red is shown in top right inset. Two arcs indicate fiber texture along [110] and [200] directions. Bottom inset is a higher magnification of top left corner showing frayed nfs in a direction that is in accordance with the arcs. (b) STEM showing individual filaments, the width of which is ≈ 10 Å. Bottom inset shows nfs being chemically "drawn out" from a large central Ti_3AlC_2 particle. (c) AFM of TCO self-assembled nanofilaments derived from TiC heated in TMAH at 80 °C for 3d and washed with water. (d) Same as (c) but after diluting the colloidal suspension 500x and drop casting on a glass slide. Inset shows height profile corresponding to blue line in (d); thinnest filaments are ≈ 1.5 nm high.

both inset and main micrograph. Importantly, they are in the same directions as the frayed fibers seen at the sheet edges in top left and reproduced in lower inset. Note that the locations where arcs were observed were limited. The regions where three rings were observed were much more ubiquitous, which implies the presence of smaller nfs that are pointing in all directions. Along the same lines, the presence of truly amorphous regions cannot be discounted at this stage.

The scanning transmission electron microscope (STEM) micrograph (Fig. 3b) clearly shows the fibrous nature of the sample. The width of individual nfs is estimated to be ≈ 1 nm. Since their thickness is ≈ 5.9 Å (Fig. 1c), it follows that we are dealing with nfs roughly 6x10 $Å^2$ in cross-section that can be micrometers long (see inset in Fig. 3b and Fig. S4c). Other TEM micrographs are shown in Fig. S4. We note in passing that the theoretical surface area of these nfs is > 1500 m^2/g.

Fig. 3c and Fig. S5 show TEM and atomic force microscope (AFM) maps of a TiC-derived sample (5d at 80 °C, water washed), spin coated on glass. The fibrous nature of the product and its tendency for self-alignment are obvious. When the same suspension was diluted 500X and drop cast, individual nfs separated (Fig. 3d). An AFM trace along the blue line in Fig. 3d shows that the thicknesses, or heights, of the thinnest ribbons were ≈ 1.5 nm (inset in Fig. 3d).

To determine the number of Ti-layers per filament, we used first-principles calculations to predict the LPs. For this, relaxations were performed for three supercell structures consisting of 2- (not shown), 4- (Fig. 1c), and 6-Ti (Fig. S6a) layers, with the lowest energy anatase (101) surfaces [16] bounding the top and bottom. (Note our coordinate system is different than anatase's; here the c-axis is the stacking direction. See crystallography section in SM). We then replaced every 2O atoms by a C atom in the slab centers for an overall chemistry of $TiO_{2-2x}C_x$ where x is 0.25 or Ti_4O_6C. This was done to account for structural C *and* render the structure dynamically stable (Fig. S6b). All other configurations resulted in dynamic instabilities. As shown in inset in Fig. 1d, the LPs of the b axes of the three structures are in good agreement with experimental values especially given that the DFT calculations were performed at 0 K. However, a large increase in the *a*-LP is observed – that is closer to the experimental values – when the number of Ti layers increases to 4 or 6 (blue curves in inset in Fig. 1d). The thicknesses of the 4- and 6-layered ana-

tase are ≈ 5.9 Å and ≈ 8 Å, respectively. The diameter of a TMA cation ranges from 4.5 to 6 Å [17,18]. Using the low end, the *d-spacing* between filaments for the 4- and 6-layered structures would be 10.4 Å and 12.5 Å, respectively. Using the high end, results in a *d-spacing* (11.9 Å) for the 4-layered structure that agrees quite well with the 11.5 *d-spacing* obtained from XRD (inset in Fig. 2a and Fig. S2a). Said otherwise, the experimental value is consistent with a 4-layered structure; the 6-layered one is too thick.

Raman spectroscopy of a number of FFs (Fig. 2b) show that all peaks belong to anatase regardless of precursor chemistry [15,19].

To elucidate the flakes' chemistry a comprehensive X-ray photoelectron spectroscopic (XPS) study (Figs. S7- S9 and Table S4) was carried out. The Ti, O binding energies were found to be weak functions of precursor chemistry (Fig. S7), washing protocol, or even heating to 800 °C in Ar (Fig. S8a). This confirms once again the chemical similarities of all films. Further evidence for a bottom-up approach is that – except for Ti_3SiC_2-derived films, that show a small Si peak – all others XPS spectra were comprised of only three elements – Ti, C and O – *regardless* of starting precursor (Fig. S9).

Unfortunately, as discussed in XPS section in SM, it was not possible to quantify the C-content in our flakes. Electron energy loss spectroscopy (EELS) of several TiC-based flakes indicated a Ti:C:O atomic ratio of ≈ 1:1:1 (Fig. 2c and Table S5). The flakes incorporated small amounts of N that are ignored going forward for simplicity. It is crucial to note here that both energy-dispersive X-ray spectroscopy (EDS) in the SEM and TEM confirmed a Ti:O ratio of ≈ 1.0 (Table S6). Based on this ratio, and if no C were in the structure, the Ti-oxidation state would have to be ≈ +2, which is belied by X-ray absorption near edge structure (XANES) measurements (Fig. 2d) at the Ti K-edge on TiC-derived films that indicate that the average oxidation state (AOS) is between +3 and +4. What renders the problem more formidable is that in all cases the O:Ti ratio in XPS was closer to 3 than 1 (Table S7). Why the XPS and EELS results do not agree remains the subject of ongoing work.

To better understand the chemistry of our flakes a thermogravimetric analysis (TGA) in Ar up to 800 °C on select films was carried out. The results are shown in Fig. S10a. With the notable exception of the TiO_2-derived films, in all other cases there were two major weight loss events when LiCl washed films were heated. One before ≈ 200 °C and another at ≈ 300 °C or higher temperatures. For the TiB_2, TiC and Ti_3SiC_2-derived films, the latter is quite sharp. In most cases the weight loss at ≈ 300 °C was about 4%. The weight losses at >300 °C for the Ti_3AlC_2- and TiN-derived films are more diffuse, but the total was still ≈ 4 %. The sharpness of the weight loss event at 300 °C is better seen in Fig. S10b, for a TiC-film heated in *air* to 800 °C. In that run, the TGA was equipped with a mass-spectrometer, the results of which are shown in Fig. S10c. It follows that the only gas released up to 400 °C is water. The first is most probably weakly bound interlayer water; the second may be water of hydration associated with the Li ions and/or more likely dehyroxylation. The lack of higher atomic number species indirectly attests to the fact that the LiCl washing step rids the interlayer space of TMA cations and other reaction products. Not surprisingly the weight losses of films washed with only ethanol were higher (red curve in Fig. S10a).

After the TGA runs, we obtained XRD patterns of the resulting powders (Fig. S11). Rietveld analysis of tthese patterns resulted in the results listed Table S8. In all cases, two major phases were identified: a Li-titanate, LT, phase – $Li_{1.33}Ti_{1.67}O_4$ – and rutile or anatase. In the case of Ti_3AlC_2, Ti_3SiC_2, TiC precursors the molar ratio of the TiO_2/LTA was ≈ 7:3; for TiB_2 the ratio was closer to 1:1; for TiO_2 there is little LT. Note that the higher the Li content the higher the Ti^{3+} fraction in the films. Our approach can thus be used to tune the Ti^{3+}/Ti^{4+} ratio, an important consideration in many applications.

Washing with ethanol alone and heating the films in Ar to 800 °C, no Li-containing phases are obtained. The presence of a LT phase thus implies that cations (TMA^+ and/or protons) between the layers are exchanged by Li during the LiCl washing step in a fashion quite reminiscent of our MXene work [20,21]. The TiO_2-derived samples were only lightly lithiated, even after washing with LiCl (Table S8), because in this case the material is *not* layered (see Fig. S12). This sample's TGA (black curve in Fig. S10a) is an outlier for the same reason. Cationic exchange eliminates the possibility we are dealing with layered double hydroxides. The absence of a Cl signal in XPS (see Fig. S9b) also supports this conclusion.

Based on the EELS, XANES, DFT and TGA results it is reasonable to assume that the chemistry of flakes is given by $Z_\delta(Ti^{4+})_{1-\delta}(Ti^{3+})_\delta\ O_{2-2x}C_x$, with x <1.0. Z is a cation that accounts for the fact that the Ti-oxidation state is <4+. Said otherwise, the decrease in oxidation state must be balanced by cations. Note this conclusion is predicated on the nfs having no defects, a very unlikely scenario. The fact that many of the films are dark gray to black strongly suggest the presence of defect states in the band gap.

The overall situation is even more complex. For example, in some regions, the Ti:X ratio obtained from EELS, where X = O + C + N approaches 1 (see spots 1 and 5 in Table S5). It is hereby acknowledged that what we are dealing with is a quite complex system that is not necessarily homogenous and will require much work to decipher. These comments notwithstanding, our conclusions concerning the structure of the flakes and the presence of C in the structure remain valid.

Before discussing properties, it is useful to discuss the mechanisms involved in the formation of the nfs and 2D layers. Chen et al. – starting with tetra-n-butyl titanate and TMAH – concluded that the presence of TMAH provides an organic cation to assist and direct the Ti-octahedra polycondensation process that resulted in the regular arrangement of rectangle nanocrystalline anatase particles they observed [15]. Tan et al. treated $TiCl_4$ hydrothermally at 125 °C as a function of time [19]. After 1 and 4 h reaction times, their XRD patterns are - but for the location of the (240) near 60° 2θ – *identical* to the ones shown Fig. 2a. When they increased their reaction times to 12 h and 24 h, their 2D material converted to bulk anatase. They proposed a model where the TMAH helps in assembling the Ti octahedra into 2D layers, while simultaneously intercalating the resultant sheets. There is no reason to believe that this mechanism does not apply here as well, except that because we are working at temperatures low enough that the TMA molecules are more stable [22], our material does *not* transform to bulk anatase. Lastly, in contradistinction to all previous work, herein the TMAH not only caps the

low energy (00l) planes [19], but must also cap a second surface perpendicular to the growth direction. This creates a situation where growth is confined to one dimension. Inset in Fig. 3b and Fig. S4f suggest that the filaments are chemically "drawn" out of the precursor and the polycondensation process maybe occurs at that interface. Once the nfs are formed they must self-assemble into 2D flakes. Fig. S4d is a snapshot of how, in certain regions, the nfs self-align to form "crystalline" regions.

Films derived from TiC and the MAX phases were conductive, with conductivities in the range of 0.01–0.05 S/cm; those made with TiO_2 or TiB_2 were not. These conductivities are roughly 5–6 orders of magnitude lower than MXenes, that range from 2000 to 25,000 S/cm, but notably *orders of magnitude higher* than typical oxides, especially the more common version of layered titanates, viz. lepidocrocites [23–25]. The conductivity is not always present and suggests an unknown variable is at play that is currently being investigated.

To shed light on the electronic structure, we measured their UV–vis optical absorption spectra from 200 nm to 800 nm. Tauc plots (Fig. 4a) of all films show a clear signature of an indirect band gap (E_g) as well as a pronounced Urbach tail due to transitions between sub-gap states. When a modified Tauc method was used to deconvolve the inter-band transitions from the contributions of disorder-related Urbach tail states [26], we concluded that the indirect band gaps fall in the 4 eV range. These values are the highest ever reported for anatase, but consistent with increases in E_g as dimensions shrink [27]. Liao et al. [28] predicted and confirmed, $E_g \approx$ 3.6 eV for their 2-Ti layered 2D anatase flakes. Our E_g is even higher because our flakes are comprised of ≈ 6x10 $Å^2$ nfs. This record E_g value for TiO_2 cannot be *overemphasized* since it indirectly confirms the extreme dimensions of our nfs. Note that at 3.3 eV, E_g of our TiO_2-derived nanoparticles is closer to that of bulk anatase as expected (Fig. 4a)

Interestingly, here there is *no* correlation between the Ti^{3+} content – as deduced from the Li concentration – and the Urbach tails as some have suggested [29]. We thus tentatively conclude that the tails, and the conductivity, arise from point defects. In some of the EELS measurements, the Ti fraction approaches 0.5 (Table S5) which suggests that O/C vacancies form. This comment notwithstanding, more work is needed to understand why some of these films are sometimes conductive.

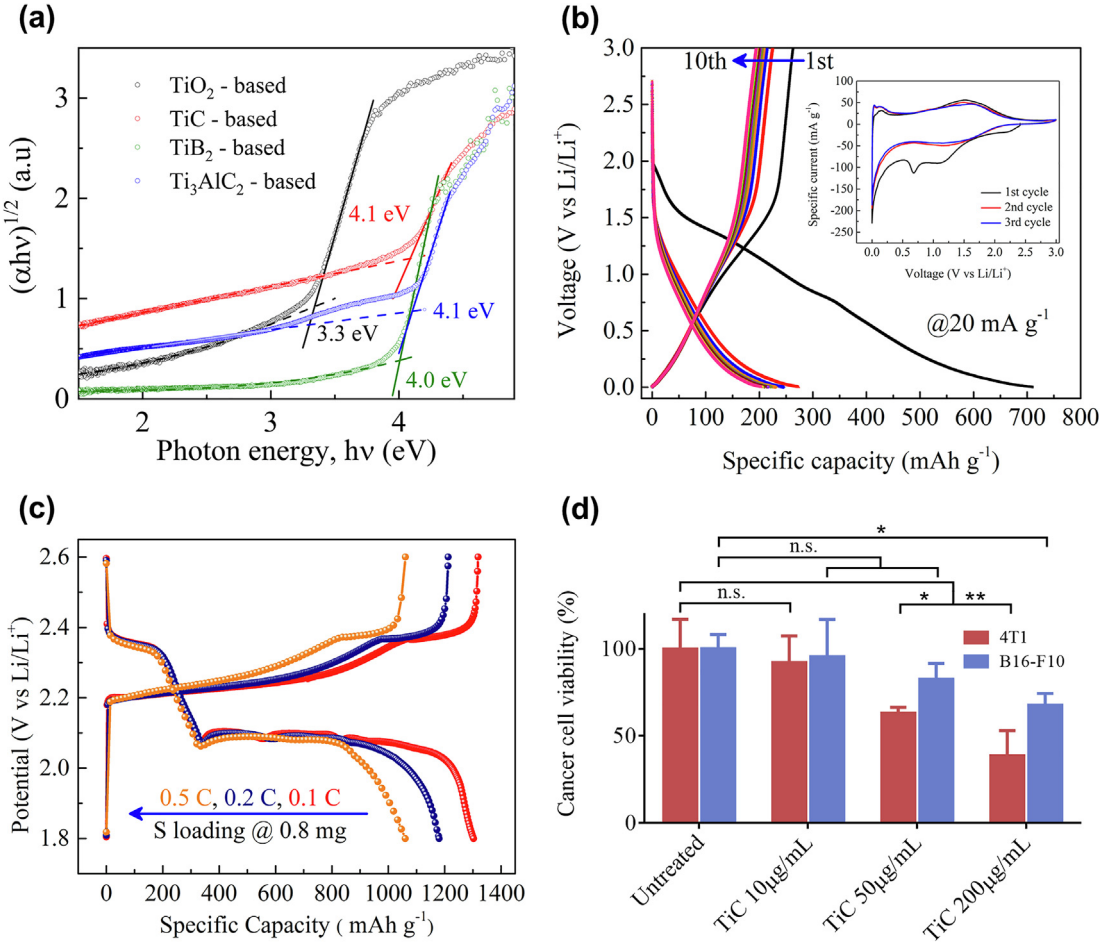

FIGURE 4

(a) Tauc plots of various precursor-derived films. Dashed lines model baseline due to Urbach tail absorption; solid lines are fits to linear parts. Charge-discharge curves of, (b) Voltage profile for Ti_3AlC_2-derived electrode material when tested in LIBs at 20 mA g^{-1}; inset shows cyclic voltammogram at 0.1 mV s^{-1}, (c) Charge–discharge curves of TCO cathode at various current rates in Li–S cell. (d) Cancer cell (see text) viability. Values indicate mean ± SD (n = 3); *p < 0.05, **p < 0.01.

To investigate possible applications, we tested the performance of our 2D flakes in lithium-ion batteries (LIBs) and lithium-sulphur (Li-S). The results are shown in Fig. 4b and c, respectively and in both cases, the results are promising. A detailed discussion can be found in SM (see Figs. S13 and S14). In the LIB case, the absence of lithiation and delithiation peaks at 1.64 V and 2.1 V in the cyclic voltammograms (CV), (inset in Fig. 4b) confirm that this electrode is neither TiO_2 nor a layered titanate [30,31]. Moreover, the Coulombic efficiency of the electrode was ≈ 99.3% after 200 cycles (Fig. S13d), reflecting highly efficient electrochemical cycling.

The Li-S coin cells with a Li anode and a TiC-derived TCO cathode were assembled and cycled. Results are shown in Fig. 4c and are discussed in detail in SM.

Crucially these results are included here simply as *proof of concept* to confirm the 2D nature of the materials obtained and their potential. However, it is reasonable to assume these results can be greatly enhanced with better understanding of what is obtained. These comments notwithstanding, it is hereby acknowledged that much more work, clearly beyond the scope of this paper, is needed to understand the mechanisms, involved, etc. However, it is fair to say, that these materials show great promise, especially as Li-S cathodes. For example, as shown in Fig. S14b, the capacity was constant at ≈ 1000 mAh/g for about 300 cycles before fading.

Lastly, to further demonstrate the versatility of our TCOs we explored their potential for biomedical application and indeed there is promise there in cancer therapy (Fig. 4d). Here mouse 4 T1 breast cancer cells and B16-F10 melanoma cells were treated with different concentrations of TiC-derived TCOs for 24 h before a MTT assay was used to measure their viability. At a concentration of 200 μg/ml, the TCO particles could induce cancer cells' death, and were more effective on the 4T1 breast cancer cells than to B16-F10 melanoma cells.

Conclusion

We discovered a simple, inexpensive, relatively high-yield, near ambient, fully scalable, one-pot, bottom-up approach to fabricate 2D anatase-based titanium carbo-oxide films comprised of nfs. By heating 11 different - layered and non-layered Ti-based precursor powders in TMAH at different temperatures (25–85 °C) for various times we converted 10 of them to 2D flakes that are anatase-based and are in turn comprised of ≈ 6 × 10 $Å^2$ nanofilaments with substantial C-content. Several of the films were dark in color and sometimes conductive, with conductivities in the 0.01–0.05 S/cm range. However, since there was no correlation between the Urbach tails and the fraction of Ti^{3+} as deduced from the overall Li content, we conclude that the source of the conductivity is not the reduced oxidation state but probably point defects. The TCOs performed well as electrodes in LIB and Li-S batteries. They also show potential in biomedical applications.

Materials and methods

Processing of films

Our synthesis process entails immersing precursor powders in 25 wt.% TMAH in polyethylene jars that are heated on a hot plate at temperatures that ranged from room temperature (RT) to 85 °C and for durations from 24 h to a week. After reaction with the TMAH, (except for Ti_2SbP, TiB_2 and TiO_2) a dark black sediment was obtained, collected, and rinsed with ethanol, shook, and centrifuged at 3500 rpm for multiple cycles until a clear supernatant was obtained. Once the supernatant was clear, 30 mL of deionized, DI, water was added to the washed products and shook for 5 mins. After centrifugation at 3500 rpm for 0.5 h, without sonication, a stable colloidal suspension was obtained. Any unreacted powders settled down. The colloid was then vacuum filtered to produce FF some of which were characterized.

In some cases, an additional step of washing with LiCl solution was conducted and the produced flakes were characterized. A 5 M LiCl solution was added to the black colloidal suspension obtained above. This resulted in deflocculation. The sediment was shaken and rinsed with deionized water through centrifugation at 5000 rpm for three cycles. The LiCl/DI water washing process was repeated until the pH was ≈ 7. The washed sediment was then sonicated in a cold bath for 1 h under flowing Ar, shaken for 5 min, then centrifuged at 3500 rpm for 10 min. The colloidal suspension was filtered to produce FFs. The FFs were then left to dry in a vacuum chamber overnight before further characterization.

In few cases, the black slurry – produced from the reaction of TMAH and TiC – centrifuged (at 5000 rpm for 5 min) directly without the addition of any solvents, the supernatant decanted, the sediment resuspended in 20 mL DI water, shook for 5 min, then centrifuged at 3500 rpm for 30 min. The produced black colloidal suspension was used for XRD (not shown) and TEM imaging.

The yield was calculated as fraction of the number of moles of Ti in the produced anatase-like structure (molar mass of TiO_2 is used for simplicity) to those supplied by the precursor. For instance, the yields for TiC and Ti_3AlC_2 are 19% and 28%, respectively. In general, the yield is of the order of ≈ 20% depending on starting precursor. The solid loading in our colloidal suspensions is of the order of 10 g/L.

X-ray diffraction, XRD

XRD patterns on air dried samples were acquired using a powder diffractometer (Rigaku SmartLab) setup in the Bragg–Brentano geometry with Cu Kα radiations in the 2–65° 2θ range using a 0.02° step size and a dwell time of 1 s/step. We also obtained XRD patterns, in transmission mode, on vertically oriented films.

Raman Spectroscopy, RS

Raman scattering spectra were collected at 300 K in air from FF of a number of precursors (Fig. 2b). The samples were probed using a 532 nm laser emitting 3.75 mW of power at the sample and focused to a spot diameter of ~0.5 μm. Scattered light was collected in a backscattering geometry and was dispersed and detected using a single-axis monochromator equipped with a charge-coupled detector array (Horiba XploRA, Edison NJ)

X-ray photoelectron spectroscopy, XPS

XPS was performed using a spectroscope (VersaProbe 5000, Physical Electronics, Chanhassen, Minnesota). Monochromatic Al-Kα X-rays with a 200 μm spot size were used. A pass energy of 23.5 eV, with an energy step of 0.05 eV and a step time of

0.5 s was used to gather high-resolution spectra. The number of repeats per scan was 10. XPS spectra were calibrated by setting the major C–C peak to 285.0 eV. Peaks were fit using asymmetric Gaussian/Lorentzian line shapes. The background was determined using the Shirley algorithm. All samples were mounted on a XPS stage using carbon tape.

Scanning electron microscope, SEM

Micrographs and elemental compositions were obtained using a SEM, (Zeiss Supra 50 VP, Carl Zeiss SMT AG, Oberkochen, Germany), equipped with an energy-dispersive X-ray spectroscope (EDS, Oxford EDS, Oxfordshire, United Kingdom). The EDS values reported represent the average of at least two measurements at low magnifications of randomly selected areas with an accelerating voltage of 15 kV and 60 s dwell time.

Atomic force microscopy, AFM

Thicknesses of filaments and flakes were obtained with an AFM (Multimode 8 AFM, Bruker Nano Surfaces). A peak force tapping AFM imaging mode was applied to acquire the surface morphology and height profiles. The scanning was conducted with ScanAsyst-Air Silicon Nitride Probes at a scan rate of 0.6 Hz. Topographic images were recorded as the resolution of 256 * 256 pixels and analyzed by Nano Scope Analysis software.

Transmission electron microscope, TEM

TEM imaging and electron diffraction patterns were collected using a JEOL JEM2100F field-emission TEM. The TEM was operated at 200 keV and has an image resolution of 0.2 nm. Images and diffraction patterns were collected on a Gatan USC1000 CCD camera. Scanning transmission electron microscopy, STEM, was carried out in the Linköping monochromated and double Cs corrected FEI Titan^3 60–300 operated at 300 kV.

Electron energy loss spectroscopy, EELS

STEM-EELS spectra were acquired by averaging 100 spectra, acquired for 1 s each at a 0.25 eV/channel energy dispersion, and a collection semi-angle of 55 mrad of employed Gatan GIF Quantum ERS post-column imaging filter. Elemental quantification of present edges was performed using built in functions of Digital Micrograph.

X-ray absorption near edge structure, XANES

The Ti K-edge isotropic XANES spectra were recorded at 54° from the normal to the film using circularly polarized x-rays provided by the first harmonic of the HELIOS-II type helical undulator (HU-52). The x-ray beam was monochromatized using a fixed-exit double crystal monochromator equipped with a pair of Si (111) crystals. Total fluorescence yield signal was collected by a Si photodiode mounted in a back-scattering geometry. Spectra were corrected for self-absorption effects. The samples were ≈ 1 mm thick compressed powered pellets. The isotropic XANES spectra were normalized to an edge jump of unity far above the absorption edge. The photon energy scale was calibrated using the pre-peak maximum in the absorption spectrum of a Ti thin foil that was set to 4965.6 eV. Spot size was 0.4 × 0.3mm^2. Experiments were performed at the European Synchrotron Radiation Facility (ESRF) ID12 beamline in Grenoble

Electrical resistivity

Electrical resistivity measurements were performed using a four-point probe device (Loresta-AX MCP-T370, Nittoseiko, Japan) at RT, then converted into electrical conductivity values.

Thermogravimetric Analysis, TGA

A thermobalance (TA Instruments Q50, New Castle, DE, USA) was used for the TGA analysis. Small pieces of FF (≈ 20 mg) were heated in sapphire crucible at 10 °C/min, under purging Ar at 10 mL/min, to 800 °C. In one experiment we used a thermobalance attached to a mass-spectrometer. In these measurements a thermal analyzer (TA instruments, SDT 650, Discovery Series) coupled with a mass spectrometer (TA instruments Discovery Series) operating at 40 V ionizing potential was used. Samples were held at RT for 0.5 h then heated to 800 °C at 10 °C/min under dry compressed air flow at 50 mL/min. The carrier gasses and evolved gas products from the sample were measured by scanning over the 1–100 atomic mass unit range. The ion current for each m/z (mass/charge ratio) was normalized by the initial sample weight.

UV–vis

UV–VIS spectra were recorded using spectrophotometer (Evolution 300 UV–Visible, Thermo Scientific). Measurements were performed in transmission mode on 1–10 μm thick films coated onto quartz slides.

DFT calculations

First-principles calculations were carried out using the Vienna *ab initio* simulation package (VASP) [32]. The projector-augmented wave (PAW) method was used together with a plane wave basis expanded to a kinetic energy cutoff of 600 eV. Exchange-correlation effects were described within the generalized gradient approximation using the Perdew, Burke and Ernzerhof (PBE) functional [33]. Brillouin zone integration was performed using the Gaussian smearing method with a smearing width of 0.05 eV. The electronic configurations of the pseudopotentials used were C: [He]2s^{2}2p^2, O: [He]2s^{2}2p^4 and Ti_sv: [Ne] 3s^{2}3p^{6}3d^{2}4s^2. The calculation supercells were constructed to consist of various anatase (101) atomic layers using a slab model, with periodicity along the *a* and *b* axes of the supercell, which correspond to the [100] and $[10\bar{1}]$ directions of bulk anatase, respectively. The supercell geometry and atom positions were relaxed until the force on each atom <5 meV/Å. A vacuum region of 15 Å was added along the c-axis (in the new coordinate system) of the supercell to eliminate interactions between periodic images perpendicular to the slabs. For the structural optimization, the first Brillouin zone was sampled by a 16x6x1 k-point sampling, while a 8x3x1 supercell together with a 2x2x1 k-point sampling was used for the phonon calculations.

Electrochemical measurements

Lithium ion battery, LIBs

To evaluate the electrochemical performance of TCO as electrodes in LIBs, we tested them in half-cell configurations against Li metal. The TCO working electrodes were fabricated by drop-casting a slurry of active materials with binder and carbon additive on a carbon coated copper foil. The slurry was prepared by

mixing 40.0 mg of active materials, 5.0 mg of poly(vinylidene fluoride) (PVDF, Sigma Aldrich, US) binder in N-methyl-2-pyrrolidinone (NMP, 99.5%, Acros Organics, Extra Dry over Molecular Sieve, Germany) solvent, and 5.0 mg of carbon black. The as-prepared electrodes were dried overnight at 60 °C. The electrode mass loading was ~1.2–1.5 mg/cm^2. Two-electrode CR2032-type coin cells were assembled in an Ar-filled glovebox with O_2 and H_2O <0.1 ppm. Li metal foil was used as a counter electrode. 1 M $LiPF_6$ in ethylene carbonate (EC)/ethylmethyl carbonate (EMC) with 3:7 (by weight) and glass fibers were used as electrolyte and separator, respectively. CVs and galvanostatic charge–discharge tests were performed with a cut-off electrochemical voltage window of 0.001–3.0 V vs Li/Li$^+$ using an electrochemical workstation (BioLogic VMP3) and a cycler (Landt CT2001A). Electrochemical impedance spectroscopy with frequency from 100 kHz to 10 mHz were conducted in a electrochemical workstation (BioLogic VMP3).

Sulphur-lithium cells

To evaluate the performance of TCOs as sulfur hosts in Li-S batteries, we prepared TCO/S cathodes using a slurry-based method. Briefly, the slurry was prepared by mixing 35 wt% vacuum-dried TCOs, 35 wt% sulphur, S, with 20 wt% conductive carbon (Alfa Aesar, Super P) and 10 wt.% battery grade PVDF binder (MTI Corp., USA). The materials were hand-ground with a mortar and pestle until the mixture appeared uniform. Later, N-Methyl-2-pyrrolidone (TCI, USA) was slowly added until the required visible consistency and uniformity of the slurry were achieved (~25 minutes). The slurry was later cast on aluminum foil using a doctor blade (MTI Corp., USA) with a thickness of 20 μm. Once cast, the slurry was kept in a closed fume hood for 2 h before transferring to a vacuum oven where it was dried at 50 °C for 12 h.

The dried TCO/S cathodes were cut using a hole punch (diameter 11 mm) to form disks. The electrodes were then weighed and transferred to an Ar-filled glove box (MBraun Lab star, O_2 < 1 ppm, and H_2O < 1 ppm). The CR2032 (MTI Corporation and Xiamen TMAX Battery Equipment) coin-type Li–S cells were assembled using TCO/S cathodes, a 15.6 mm diameter, 450 μm thick Li disk anode (Xiamen TMAX Battery Equipment) a tri-layer separator (Celgard 2325), and a stainless-steel spring and two spacers along with the electrolyte. The electrolyte, with 1 M LiTFSi with 1 wt% $LiNO_3$ in a mixture of 1,2-dimethoxyethane and 1,3-dioxolane at a 1:1 volume ratio, was purchased (TMAX Battery Equipment, China). According to the manufacturer the electrolyte contained trace amounts of oxygen and moisture (H_2O < 6 ppm and O_2 < 1 ppm). Assembled coin cells were rested at their open-circuit potential for 10 h before performing the electrochemical experiments at RT. Cyclic voltammetry was performed at a scan rate of 0.1 mV.s^{-1} between voltages 1.8 and 2.6 V wrt Li/Li$^+$ using a potentiostat (Biologic VMP3). Prolonged cyclic stability tests were carried out with a battery cycler (Neware BTS 4000) at different C-rates (where 1 C = 1675 mAh.g^{-1}) between voltages of 1.8 and 2.6 V. The Li–S cells were conditioned for 2 cycles at 0.1 C and 0.2 C, before undergoing long cycling at 0.5 C.

Biological tests

One day before treatment, 4T1 and B16-F10 cells were added into a 96 well plate at a density of 10,000 cells/well. The cells were cultured at 37 °C/5% CO_2 in RPMI-1640 medium supplemented with 10% fetal bovine serum and 100 IU/mL penicillin/streptomycin for 24 h. The cells were then treated with TiC-based TCOs at concentrations of 10 μg/mL, 50 μg/mL or 200 μg/mL. After 24 h treatment, a thiazolyl blue tetrazolium bromide (MTT) assay was performed according to manufacturer's protocol. The absorbance at 570 nm and 630 nm was measured. Relative cell viability was obtained by comparing to the absorbance of untreated cells. All measurements were performed in triplicate. Data was analyzed using two-way ANOVA with post-hoc Tukey's test.

Declaration of Competing Interest

The authors declare that they have no known competing financial interests or personal relationships that could have appeared to influence the work reported in this paper.

Acknowledgements

XRD, XPS, SEM and TEM analyses were performed using instruments in the Materials Characterization Core at Drexel University. We thank Dr. Dmitri Barbash for his assistance with the XRD. We would like thank Mr. Mark Anayee for the air TGA-MS run. Computations were done at Drexel's University Research Computing Facility as well as the National Supercomputer Centre, Sweden, allocated by the Swedish National Infrastructure for Computing (SNIC).

Funding

This work was funded by the Ceramics Division of NSF (1740795) and Murata Manufacturing Co. Ltd of Japan. WPI team acknowledges support from WPI TRIAD Seed Grant. We acknowledge support from the Knut and Alice Wallenberg (KAW) Foundation for funding and for support of the Linköping Electron Microscopy Laboratory. Dr. Yong-Jie Hu acknowledges the financial support from his startup fund from Drexel University and the computational support from Drexel's University Research Computing Facility. Prof. Per Persson acknowledges the Swedish Foundation for Strategic Research (SSF) through the Research Infrastructure Fellow program no. RIF 14-0074. Rahul Pai and Dr. Vibha Kalra acknowledge support from NSF funding No. 1919177.

Author contributions

H.O.B. and M.W.B. conceived the idea and designed the experiments. H.O.B., M.Q.H., and K.M. carried out synthesis. H.O.B. carried out most of the XRD, SEM, EDS, and TEM-EDS characterization. T.E.M. and C.L. carried out the XRD analysis and helped with structural refinement. M.C. did the TGA analysis. V.N., J.L.M., and R.L.G. carried out XPS analysis. O.W, A.M, H.O.B., A.K., J.L.M., R.L.G., and M.W.B. proposed conversion chemistries consistent with the data. A.K., A.R., and S.M. carried out the Raman measurements. K.L., M.N., R.P., and V.K. carried out the electrochemical work and analysis. C.J., H.O.B., C.L., P.P., and J.R. carried out TEM and EELS and analysis. Q.Q and C.L. carried out AFM. K.K., E.C.U., L.V.T., and R.L.G. carried out UV-vis experi-

ments and analysis. Y.Z. and H.C. carried out biological testing. T.T., M.K., and A.Y. helped with discussions. T.O., M.B., F.W., and A.R. carried out the XANES measurements. Y.-J.H., J.R, and J.B. carried out DFT analysis. M.W.B also supervised the project and wrote the manuscript. All authors discussed the results and commented on the manuscript.

Data and materials availability

All data, and materials used in the analysis must be available in some form to any researcher for purposes of reproducing or extending the analysis.

Appendix A. Supplementary data

Supplementary data to this article can be found online at https://doi.org/10.1016/j.mattod.2021.10.033.

References

[1] K.S. Novoselov et al., Science 353 (2016) 461.
[2] D. Deng et al., Nat. Nanotechnol. 11 (2016) 218–230.
[3] K.S. Novoselov, Science 306 (2004) 666–669.
[4] K.S. Novoselov et al., PNAS 102 (2005) 10451–10453.
[5] F. Xia, H. Wang, Y. Jia, Nat. Commun. 5 (2014) 4458-4458..
[6] M. Naguib et al., Adv. Mater. 23 (2011) 4248–4253.
[7] L. Verger et al., Curr. Opin. Solid State Mater. Sci. 23 (2019) 149–163.
[8] S.L. Swartzen-Allen, E. Matijevic, Chem. Rev. 74 (1974) 385–400.
[9] L. Verger et al., Trends Chem. 1 (2019) 656–669.
[10] T. Yang et al., Adv. Mater. Interfaces 6 (2019) 1801160.
[11] Z. Sun et al., Nat. Commun. 5 (2014) 3813.
[12] J. Xuan et al., Angew. Chem. (2016).
[13] D.N. Miller et al., J. Mater. Chem. A 4 (2016) 5730–5736.
[14] M. Ghidiu, M.W. Barsoum, J. Am. Ceram. Soc. 100 (2017) 5395–5399.
[15] Y. Chen, et al., J. Colloid Interface Sci. 310 (2007) 171-177..
[16] F. Labat, P. Baranek, C. Adamo, J. Chem. Theory Comput. 4 (2008) 341–352.
[17] Z. Liu et al., Langmuir 16 (2000) 4154–4164.
[18] S.L. Brock et al., J. Phys. Chem. B 103 (1999) 7416–7428.
[19] Z. Tan, K. Sato, S. Ohara, Adv. Powder Technol. 26 (2015) 296–302.
[20] M. Ghidiu et al., Chem. Mater. 28 (2016) 3507–3514.
[21] L. Verger et al., J. Phys. Chem. C 20044-20050 (2019) 19725–19733.
[22] X. Dong et al., Appl. Surf. 256 (2010) 2532–2538.
[23] A.D. Dillon et al., Adv. Funct. Mater. 26 (2016) 4162–4168.
[24] M. Ghidiu et al., Nature (2014).
[25] C.J. Zhang et al., Adv. Mater. 29 (2017) 1702678.
[26] P. Makuła, M. Pacia, W. Macyk, J. Phys. Chem. 9 (2018) 6814–6817.
[27] A.S.D. Wang, T. Sasaki, Chem. Rev. 114 (2014) 9455–9486.
[28] T. Liao, Z. Sun, S.X. Dou, ACS Appl. Mater. Interfaces 9 (2017) 8255–8262.
[29] D.-E. Gu et al., Chem. Commun. (2008) 2453–2455.
[30] Y. Dong et al., Adv. Funct. Mater. 26 (2016) 7590–7598.
[31] J. Xu et al., Electrochim. Acta 52 (2007) 8044–8047.
[32] G. Kresse, J. Furthmüller, Phys. Rev. B 54 (1996) 11169–11186.
[33] J.P. Perdew, K. Burke, M. Ernzerhof, Phys. Rev. Lett. 77 (1996) 3865–3868.